JGR Solid Earth

RESEARCH ARTICLE

Key Points:

- We train a ML model that utilizes HR-GNSS data to predict source parameters and shaking intensity for large (M7.0+) earthquakes
- The model yields a long median warning time of 35–40 s for MMI 4+ when tested on synthetic and real HR-GNSS records
- Our model fills a critical gap in current EEW systems for large events and can operate in parallel with other methods for better warnings

Correspondence to:

J.-T. Lin,
lin51@llnl.gov

Real-Time Fault Tracking and Ground Motion Prediction for Large Earthquakes With HR-GNSS and Deep Learning

Jiun-Ting Lin[1,2] , Diego Melgar[1] , Valerie J. Sahakian[1] , Amanda M. Thomas[1] , and Jacob Searcy[3]

[1]Department of Earth Sciences, University of Oregon, Eugene, OR, USA, [2]Lawrence Livermore National Laboratory, Livermore, CA, USA, [3]Department of Data Science, University of Oregon, Eugene, OR, USA

Abstract Earthquake early warning (EEW) systems aim to forecast the shaking intensity rapidly after an earthquake occurs and send warnings to affected areas before the onset of strong shaking. The system relies on rapid and accurate estimation of earthquake source parameters. However, it is known that source estimation for large ruptures in real-time is challenging, and it often leads to magnitude underestimation. In a previous study, we showed that machine learning, HR-GNSS, and realistic rupture synthetics can be used to reliably predict earthquake magnitude. This model, called Machine-Learning Assessed Rapid Geodetic Earthquake model (M-LARGE), can rapidly forecast large earthquake magnitudes with an accuracy of 99%. Here, we expand M-LARGE to predict centroid location and fault size, enabling the construction of the fault rupture extent for forecasting shaking intensity using existing ground motion models. We test our model in the Chilean Subduction Zone with thousands of simulated and five real large earthquakes. The result achieves an average warning time of 40.5 s for shaking intensity MMI4+, surpassing the 34 s obtained by a similar GNSS EEW model. Our approach addresses a critical gap in existing EEW systems for large earthquakes by demonstrating real-time fault tracking feasibility without saturation issues. This capability leads to timely and accurate ground motion forecasts and can support other methods, enhancing the overall effectiveness of EEW systems. Additionally, the ability to predict source parameters for real Chilean earthquakes implies that synthetic data, governed by our understanding of earthquake scaling, is consistent with the actual rupture processes.

Plain Language Summary Earthquake Early Warning (EEW) systems can evaluate the shaking impact soon after an earthquake occurs and send alerts to areas where strong shaking has not yet arrived. However, predicting shaking intensity for large earthquakes face challenges such as magnitude underestimation and rupture complexity, leading to inaccurate prediction. In our previous study, we proposed a machine learning model, called M-LARGE, which can predict the magnitude of large earthquakes accurately and rapidly by utilizing surface deformation patterns recorded by HR-GNSS. Here, we expand the M-LARGE model to also predict the source location and fault size. This capability allows us to construct a fault, enabling forecasts of strong shaking 35–40 s before the shaking onset, longer than other similar methods. Our approach has the potential to improve the accuracy of EEW and reduce the impact of seismic hazards. Because the model is fully trained with simulated data, the successful prediction of real Chilean earthquakes indicates that our assumptions in simulating large earthquakes are sufficiently consistent with the rupture dynamics of actual events.

1. Introduction

Earthquake early warning (EEW) systems aim to provide seconds to minutes of warning to the public and automated systems before strong shaking occurs at their location (Allen & Melgar, 2019; Given et al., 2014). The most commonly adopted EEW system relies on the quick estimation of point source parameters (hypocenter location and magnitude) and forecasts the upcoming strong ground motion with ground motion models (GMM) (Allen, 2007; Allen & Kanamori, 2003; Nakamura, 1988). This method has been applied or is currently in development in Japan (Kamigaichi et al., 2009; Nakamura, 1988), the west coast of the United States (Allen & Kanamori, 2003; Given et al., 2014), Mexico (Espinosa Aranda et al., 1995, 2009), Taiwan (Hsiao et al., 2009; Wu & Kanamori, 2005), Turkey (Wenzel et al., 2014), and in many other seismic active regions (e.g., Böse et al., 2007; Zollo et al., 2009).

1.1. Limitations of Current Methods

One of the challenges of the existing EEW systems is the non-point source nature of large (M7.0+) earthquakes, which possess a finite extent that can lead to source modeling errors. Such errors can result in underestimation of shaking and tsunami intensity (e.g., Hoshiba et al., 2011; Hoshiba & Ozaki, 2014). Some studies proposed finite fault methods to mitigate this issue (Böse et al., 2012; Hutchison et al., 2020). For example, the Finite-Fault Rupture Detector (FinDer) algorithm utilizes the pattern matching technique to search for fault parameters using seismic observations and a database of precomputed shaking patterns (Böse et al., 2012, 2018). Another class of algorithms that is not subject to source modeling errors is to forecast shaking intensity directly from the observed waveforms for example, Propagation of Local Undamped Motion (PLUM) model (Cochran et al., 2019; Kodera et al., 2018). Although these methods are more accurate than the original point source assumption for large earthquakes, the magnitude underestimation problem can still exist. For example, the magnitude prediction from the ShakeAlert EEW system (Given et al., 2014), a system implemented with both the point source and finite fault algorithm, underestimated the 2019 Mw7.1 Ridgecrest earthquake by 0.8 units, resulting in the underprediction of shaking levels (Chung et al., 2020). Furthermore, as noted in Kodera et al. (2018) and Cochran et al. (2019), the onsite-based algorithm either provides shorter warning times or requires a dense network to forecast intensity in a broad region.

Another challenge for EEW systems that rely on seismometers is that large earthquakes have strong, and low-frequency shaking (i.e., static offset), creating challenges in recording the true shaking observed at inertial sensors from near-field. This contributes to magnitude saturation issues (Bock & Melgar, 2016; Boore & Bommer, 2005; Larson, 2009). High-rate global navigation satellite system (HR-GNSS) data, on the other hand, provide unsaturated near-field displacement data, which are ideal for building large earthquake EEW systems. For example, one of the fastest and most stable methods, GFAST, utilizes the relationship of peak ground displacement (PGD) measured using HR-GNSS and earthquake moment magnitude (Mw) to determine the point source soon after earthquake initiation (Crowell et al., 2013, 2016). While this method is reliable, synthetic modeling shows that for unilateral ruptures, large errors are still possible (Williamson et al., 2020). Similarly, although algorithms such as G-larmS and BEFOREs aim to provide unsaturated Mw estimation (Grapenthin et al., 2014; Minson et al., 2014), they have limitations due to their reliance on the information from other seismic-based EEW systems, for example, for epicentral location (Murray et al., 2018). This means that any uncertainties in initial source estimates can cause errors in EEW performance.

Recently, a number of machine-learning (ML) approaches have emerged that can provide faster and more accurate EEW. These include using waveform data to estimate magnitude and other source parameters (e.g., Lomax et al., 2019), or directly forecasting shaking intensity from single or multi-station records in a region (e.g., Jozinović et al., 2020; Münchmeyer et al., 2021; Zhang et al., 2022). ML approaches are known to be a powerful tool for automatically extracting information from data, but their generalizability is often limited by the training data. Because large magnitude earthquakes are rare, there are only a small number of recordings available, but ML approaches require large quantities of data for model training, testing, and validation (Jozinović et al., 2020; Mousavi & Beroza, 2020; Münchmeyer et al., 2021). Recently, a number of studies have successfully used simulated data to train ML models and apply them to various applications such as computer vision, natural language processing, bioinformatics etc. (Nikolenko, 2021). In seismology, for example, Kuang et al. (2021) trained their model with 787,320 synthetic waveforms and were able to estimate the focal mechanism of four 2019 Ridgecrest earthquakes from Mw5.4–Mw7.1. The fundamental idea of the synthetic approaches is based on whether earthquakes are self-similar that is, whether a M8.0 earthquake essentially a scaled-up version of a M3.0 earthquake (Aki, 1967). This has important implications for the ability of synthetic waveforms, derived from empirical scaling relationships, to accurately reproduce actual ground motions. Although later studies have supported the earthquake self-similarity down to a specific magnitude (Abercrombie, 1995; Prieto et al., 2004), and the point source scaling approach has proven successful (e.g., Ekström et al., 2012), extracting source parameters for large earthquakes in real-time for EEW applications remains a technical challenge. Furthermore, it is unknown whether ML models can learn fault scaling beyond a simple point source (e.g., Wells & Coppersmith, 1994; Blaser et al., 2010), given the more pronounced effects of fault finiteness and the diversity of rupture patterns in large earthquakes (Hayes, 2017).

1.2. New Approaches

To address the aforementioned limitations, we developed a ML model that learned earthquake source properties from synthetic HR-GNSS records of simulated large earthquakes. The model, called Machine-Learning Assessed

Rapid Geodetic Earthquake model (M-LARGE) (Lin et al., 2021), predicts Mw evolution in real-time with a high accuracy of 99%, compared to the similar method of 80% (Lin et al., 2021). This model does not rely on source parameters from seismic methods, which may introduce saturated information. It only requires a trigger time from the existing earthquake detectors (e.g., Allen & Melgar, 2019), which is a simpler problem than source characterization. That initial attempt focused solely on earthquake magnitude; here, we report on a further expansion of the M-LARGE algorithm to predict more rapid finite fault parameters. The new algorithm estimates Mw, centroid location, and fault size simultaneously. This is a significant advancement because it enables the construction of a finite fault, which has been shown to improve the accuracy of ground motion estimations for EEW (Murray et al., 2022), and uncertainties in ground motion estimation have been shown to play a role in the accuracy of EEW alerts (Meier, 2017; Minson et al., 2019). Our approach involves a two-step process, where we first use the M-LARGE model to estimate finite fault parameters and then apply an existing GMM to predict the shaking intensity.

As a demonstration, we apply the new M-LARGE model to the Chilean Subduction Zone and test it with both the synthetic and real data from five large historical Chilean earthquakes that occurred in the past 13 years (Figure 1). The results show that the source parameters of synthetic and real Chilean earthquakes can be quickly predict, leading to sufficiently long warning times and reasonably accurate shaking intensity forecasts. Additionally, the fact that the source parameters of real Chilean earthquakes can be obtained implies that the synthetic data, produced with assumptions about earthquake scaling, is consistent with the actual source processes in recorded events.

2. Synthetic and Observed Data

We generate synthetic HR-GNSS data to train the model. The five real Chilean earthquakes (Figure 1) and a fraction of unexposed synthetic data are held for model testing. To test how well are the GM forecastings based on our model, we compare the model-predicted GM with the synthetic and real GM from Chilean earthquakes (Ruhl et al., 2019). In the following sections, we introduce the steps for HR-GNSS and synthetic GM simulations.

2.1. Kinematic Rupture Simulations

The first step in generating synthetic HR-GNSS data is rupture simulation. We take the Chilean Subduction Zone rupture and waveform data set from Lin et al. (2021), which has 36,800 rupture simulations with magnitude ranges from $7.2 < Mw < 9.4$ with a small perturbation in magnitude. The detailed methodology of the kinematic rupture simulations is described in Melgar et al. (2016) and in Lin et al. (2021). Additionally, to cover events that occur at the edge of the subduction zone, we generate a new data set of 309,600 smaller magnitude events from $7.2 < Mw < 7.7$ following the same procedures as in Lin et al. (2021). Combining with the original data set, a total of 346,400 simulated events are used in this study (Figure 2).

2.2. Synthetic HR-GNSS Waveforms

Once the kinematic ruptures have been created, the synthetic 3-components HR-GNSS waveforms can be generated by the summation of each subfault's waveform based on the Green's function approach. We use the FK package (Zhu & Rivera, 2002) and the velocity structure from LITHO1.0 (Pasyanos et al., 2014) to generate the Green's functions from all subfaults to the selected HR-GNSS stations currently operating in Chile (Báez et al., 2018). The HR-GNSS waveforms have a 1-Hz sampling rate, which is enough to cover the dominant period of large earthquakes. For computational efficiency, we only generate the waveform when the rupture is closer than 10° from the receiving station. To simulate realistic waveforms, we apply empirical HR-GNSS noise (Melgar et al., 2020) into the raw synthetic waveforms during the data augmentation step for model training, which will be described in detail in Section 3.

2.3. Synthetic High-Frequency Waveforms

The ultimate goal of EEW systems is to forecast shaking before its onset. In addition to the 1 Hz waveforms, we simulate semi-stochastic high-frequency 100 Hz broadband data at 525 virtual stations distributed along the coast, with an average spacing of 0.4°. These simulated data are considered as expected GM and will be utilized
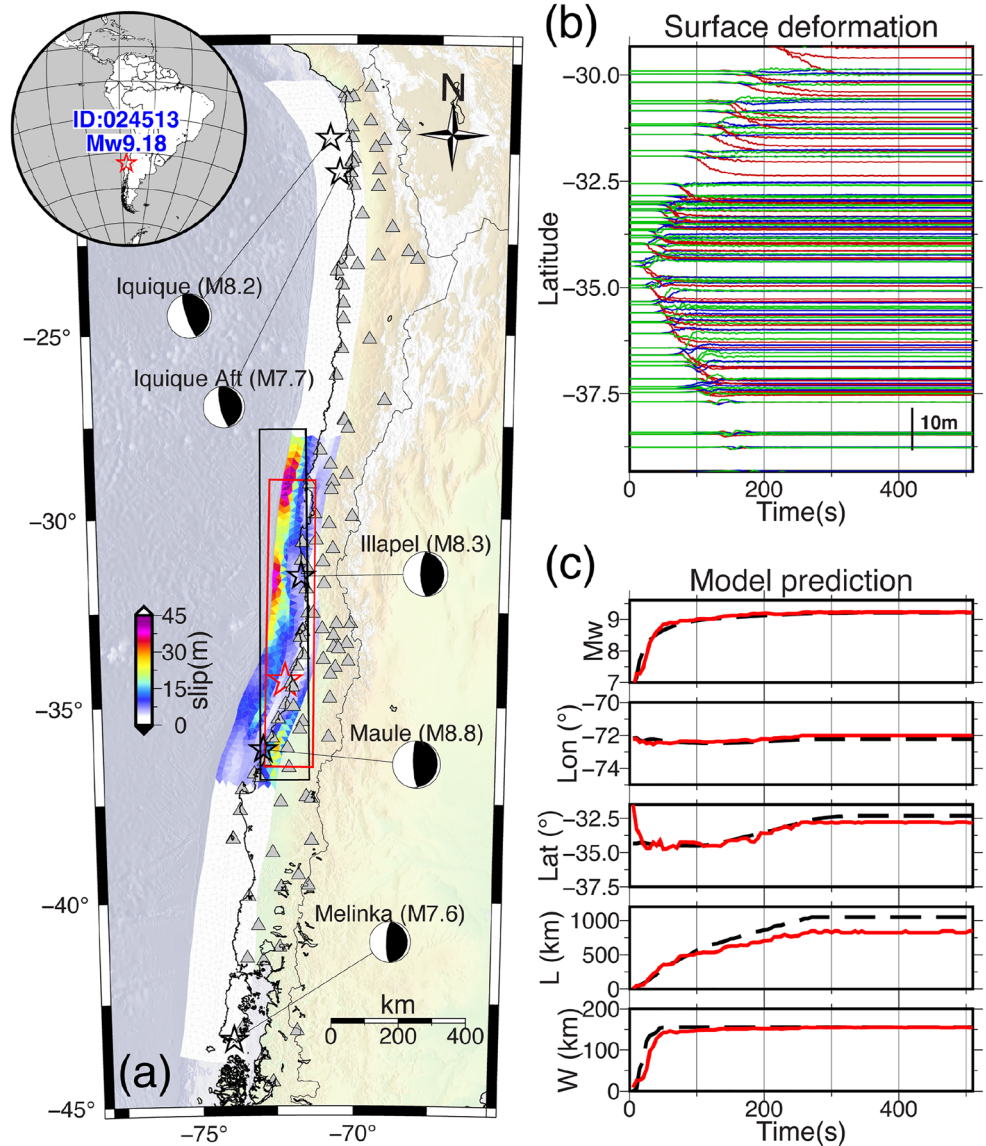
Figure 1. Map of the Chilean Subduction Zone, rupture simulation, synthetic HR-GNSS waveforms, and model prediction. (a) Simulated Mw9.18 earthquake ID:024513 from Lin et al. (2021). Red star shows the hypocenter of the synthetic earthquake. Triangles are the HR-GNSS stations used in this study. Black and red boxes mark the simplified fault of the true rupture and the model predicted fault, respectively. Black stars and focal mechanisms mark the five real large earthquakes that occurred in the past 13 years (b) Example data inputs. Synthetic 3-components HR-GNSS waveforms. Red, blue, green lines represent East-West, North-South, and vertical component, respectively. (c) Model outputs. Predicted moment magnitude (Mw), centroid longitude, centroid latitude, fault length, and fault width are shown in red solid lines. Black dashed lines show their actual values.

to test the model performance. Broadband data like this cannot be generated by the aforementioned Green's function approach because it is highly computationally expensive (e.g., Rodgers et al. (2020)). Additionally, at high frequencies, the simulations are sensitive to unconstrained small-scale crustal structures and earthquake sources. Instead, we apply the hybrid semi-stochastic approach, where waveforms are controlled by modeled amplitude spectrum and random phases (Graves & Pitarka, 2010, 2015) and as implemented by Goldberg and Melgar (2020). For computational efficiency, we randomly select the virtual stations with a distance smaller than 600 km to generate broadband data. We simulate 100 Hz broadband data for 10,000 ruptures, and compare their peak ground acceleration values (PGA) with an existing GMM for the Chilean Subduction Zone (Montalva et al., 2017) (Figure 3), which estimates GM based on Vs30 obtained from the USGS (Allen & Wald, 2009).
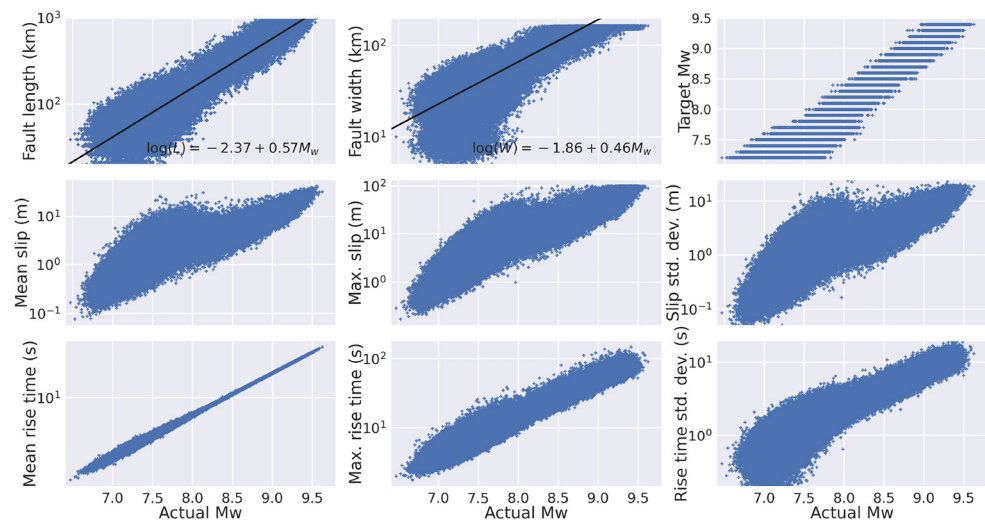
Figure 2. Rupture simulations and their source parameters. A total of 346,400 simulations are used in this study.

Overall we see no significant source or distance bias in the simulations which suggests they are reliable for use as independent testing data.

3. M-LARGE Model and Shaking Intensity Prediction

To forecast shaking intensity, we take a two-step approach similar to existing methods for example, (Allen, 2007; Allen & Kanamori, 2003; Nakamura, 1988). In which the shaking intensity is predicted based on the source parameters. Here, we begin by providing an overview of the workflow of the M-LARGE model, including the intensity prediction and the evaluation (Figure 4). We will then describe each step in detail in the subsequent sub-sections.

First, the Fakequake package (Melgar et al., 2016) generates ruptures and HR-GNSS waveforms, which are then saved into the training, validation, and testing data sets (Step (1) in Figure 4). Next, after training the M-LARGE model (Step (2) in Figure 4), we test it with both synthetic and real GNSS data to predict source parameters that are used to construct the finite fault (Step (3) in Figure 4). The fault is then utilized to predict the shaking intensity through a GMM (Step (4) in Figure 4). Before evaluating the warning time performance, we take additional steps to ensure the robustness of our stochastic simulation. Specifically, we compare the stochastic simulation with the result of GMM from the same rupture data (Step (5) and (6) in Figure 4). The comparison result is also shown in Figure 3b. Because GMM does not provide timing information about the arrival of shaking intensity at a given site, we use the simulated waveforms (Step (7) in Figure 4) to calculate the expected warning time from the model predicted shaking intensity (Step (4) in Figure 4) for the testing data set. For real earthquake data, the comparison is simply based on the real acceleration records. The additional procedure tests the overall performance of our model. However, during real EEW operations, only Step (3) and Step (8) in Figure 4 are necessary to provide warning.

3.1. M-LARGE Inputs and Outputs

In contrast to the original M-LARGE model, which utilized the PGD waveforms (i.e., PGD measurements are updated at each monitoring time) as inputs (Lin et al., 2021), here, we use the raw 3-component displacement waveforms as inputs to tackle a more intricate problem. In addition to Mw, we expand the architecture of Lin et al. (2021) to predict a total of 5 parameters: Mw, centroid longitude, centroid latitude, length, and width. The detailed model architecture is shown in Figure S1 in Supporting Information S1. The input data comprise a total of 121 Chilean GNSS stations. We add an additional channel for the station availability code to indicate whether a station is in use, resulting in a total of 484 features at each time step. We do not predict the centroid depth because depth is often not well constrained by the observations and may instead contribute as a source of noise in predicting the other parameters. Instead, we adopt the depth from the subduction zone geometry when the
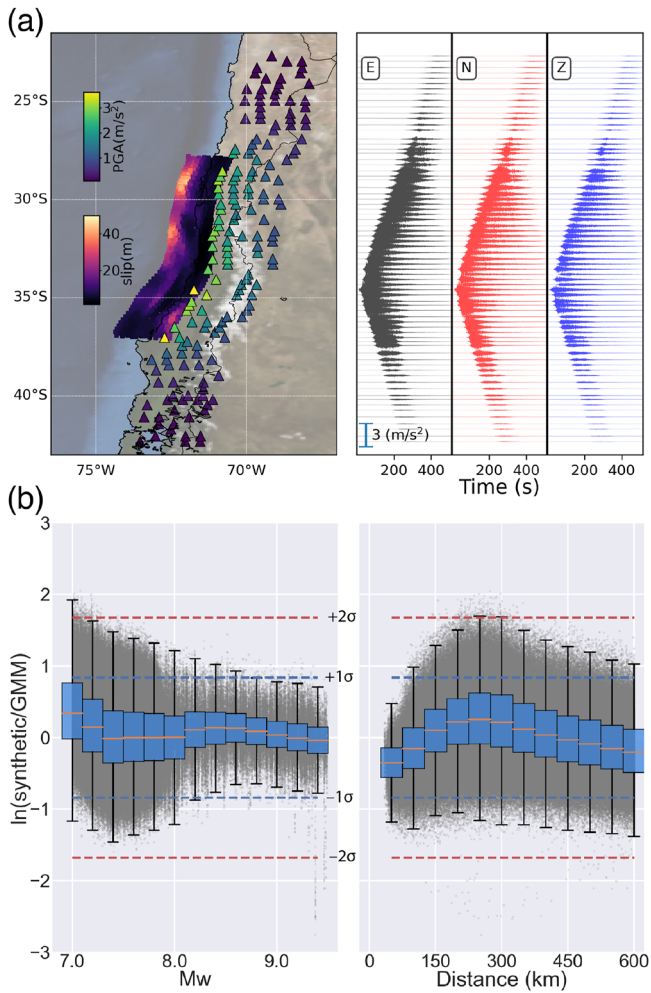
Figure 3. Examples of 3-component synthetic high-frequency waveforms and their comparison with PGA from the GMM. (a) Synthetic broadband data for rupture ID:024513 (Figure 1). Triangles represent the selected virtual stations color coded by their PGA values calculated from synthetic time series data. (b) Comparison of the synthetic broadband data and the existing GMM (Montalva et al., 2017) for different Mw (left) and distance (right) bins. Blue and red dashed lines denote the reported ±1 and ±2 standard deviations (σ) of the GMM, respectively. The result shows that the misfits are within the build-in error, and there is no significant bias for the bins.

centroid longitude and latitude are determined. Similar to Lin et al. (2021), we decimate the time series to a 5-s sampling rate, allowing the model predictions to update every 5 s up to a maximum of 510 s. The M-LARGE predicted source parameters will later be utilized to make shaking intensity prediction using an existing GMM.

3.2. M-LARGE Training and Testing

We split the total of 346,400 rupture simulations and their waveforms into 70%, 20%, and 10% for model training, validation, and testing, respectively (Figure S2 in Supporting Information S1). With these rupture simulations, we create a generator that simulates realistic data with GNSS noise and station outages following the same procedure as in Lin et al. (2021). As a result, each rupture case can have an infinite number of unique combinations of observations. We set the training batch size to 128, where the model updates its weights once based on a randomly selected group of training data generated by our generator. We train it for 300 iterations (i.e., training steps), and monitor the validation loss, this process is referred to as one training epoch. We repeat the process for 2000 epochs, during which we expose the model to a total of 76.8 million realistic data from 242,480 (i.e., 70% of the total 346,400) ruptures.

3.3. Finite Fault and Intensity Prediction

Once the source parameters are determined by the M-LARGE model, we create time-evolving finite fault planes with the strike and dip taken from subduction zone geometry (Figure 5). Next, we utilize the existing Chilean GMM (Montalva et al., 2017) to forecast the shaking intensity in PGA or in Modified Mercalli Intensity (MMI) (Worden et al., 2010) with a grid spacing of 5 m throughout the entire region. For model evaluation purposes, we select the PGA/MMI results at the 525 virtual stations used for high-frequency waveform simulations (Figure 3a). These 525 stations will be further used to quantify the misfit of shaking intensities between predicted and actual fault in the discussion. We compare the predicted shaking intensity with the actual value by

$$\text{Misfit}_t = I_t^{\text{Model}} - I_t^{\text{Actual}} \tag{1}$$

where I_t^{Model} represents the shaking intensity from either the simplified rectangular fault or M-LARGE predicted fault at time t. I_t^{Actual} represents the intensity from actual fault at time t. Here, we compare their PGA values at $t = 510$, which is the final time of our M-LARGE model. At this point, most of the ruptures have concluded, and the comparison should reflect the residual differences resulting from variations in fault geometries.

We note that due to the simplification of the fault geometry curvature, the simplified fault may introduce some errors in the MMI prediction (i.e., Figure 5); however, as we will show in the discussion, this difference is small and can be ignored. Furthermore, we recognize that there is uncertainty inherent in the ground motion estimations from the GMM (Montalva et al., 2017). However, our primary objective is not to obtain the most precise ground motion predictions. Rather, we emphasize the importance of accurate and timely source parameter prediction and how the shaking intensity can be rapidly and accurately estimated through an existing GMM.

4. Results

4.1. M-LARGE Performance on Testing Data Set

Figure 6 shows the performance of M-LARGE on 10,000 testing data, which were not used during the training process. The detailed performance with a 5-s update interval is shown in Movie S1. We define a successful prediction as the misfit of predicted and actual value being smaller than 10% of the range of each parameter. For
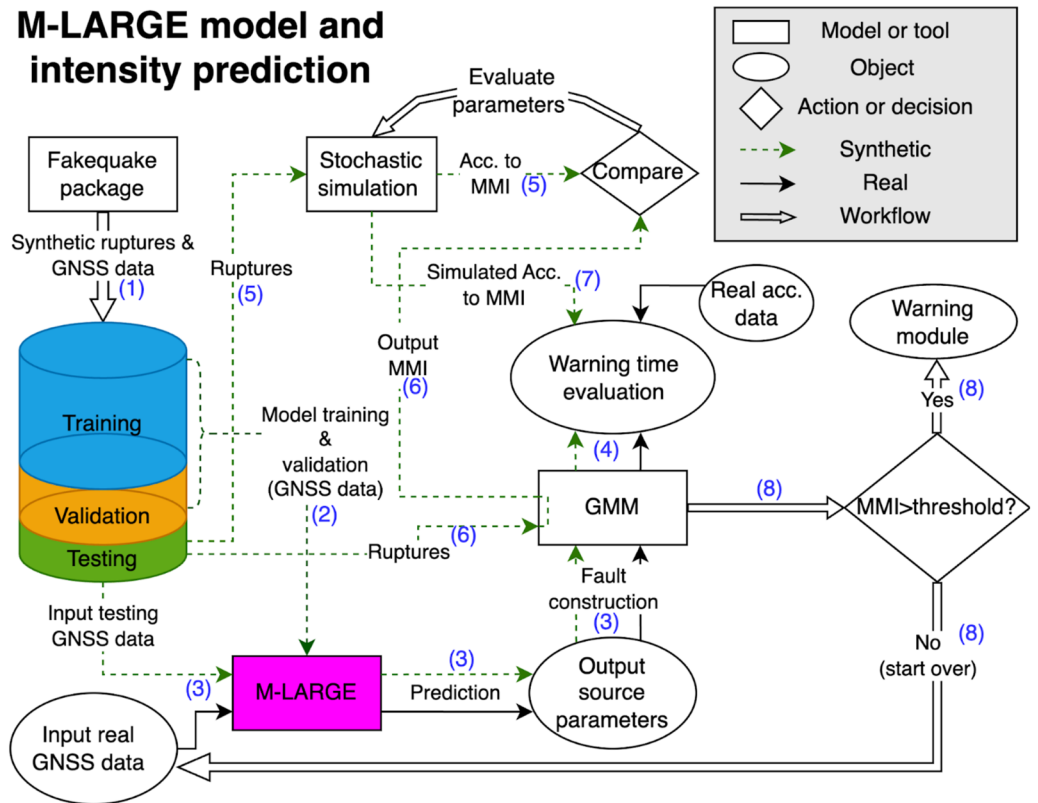
Figure 4. Flowchart for the procedure for M-LARGE model (Lin et al., 2021) and shaking intensity prediction.

example, the Mw error is set to be 0.3 Mw scale, a value obtained from the range of all the training labels from Mw6.5 to Mw9.5. We use this definition only for evaluating the model performance such that the accuracy of the predictions can be calculated. Although the accuracy of individual parameters may not be directly comparable due to differences in range and potential imbalance in their distribution, it is an important metric for assessing parameter improvements over time. Overall, the model shows higher accuracy in along-strike parameters, with an accuracy of 96.2% and 99% for latitude and length, respectively, and 93.8% and 89.4% for longitude and width, respectively. We note that when a fault grows to >1,000 km, the length value is saturated. This is due to two primary reasons. First, it is because of the simplification of the rectangular fault placed on a curved subduction zone geometry as illustrated in Figure 1. Second, there is a sparse distribution of GNSS stations across the 3,000 km long subduction zone. It is noteworthy that for larger ruptures, the availability of more GNSS stations becomes crucial in capturing the entire rupture process accurately. On average, our M-LARGE model predicts the source parameters with a high accuracy of 95.5%.

It should be noted that the performance of our M-LARGE model is evaluated under imperfect conditions where large errors and data gaps present, as demonstrated in Figure S3 in Supporting Information S1. Large outliers are usually associated with imperfect recording scenarios, including sparse station coverage and low signal-to-noise ratio. However, our test with improved data conditions such as reducing the data noise or increasing station availability suggests that the accuracy of the predictions can reach close to 100% (Figure S4 in Supporting Information S1). Our analysis also shows no strong correlation between Mw and misfits, suggesting that the network coverage and data quality are more crucial than the source complexity to the M-LARGE predictions. This is consistent with the result of Lin et al. (2021).

4.2. M-LARGE Performance on Real Data

In addition to the simulated earthquakes, we also test the model on the 2010 Mw8.8 Maule earthquake, one of the largest historical earthquakes in the Chilean Subduction Zone. Note that the availability of GNSS stations during the Maule earthquake (Figure 7) is sparsely distributed and does not reflect the current distribution of stations.
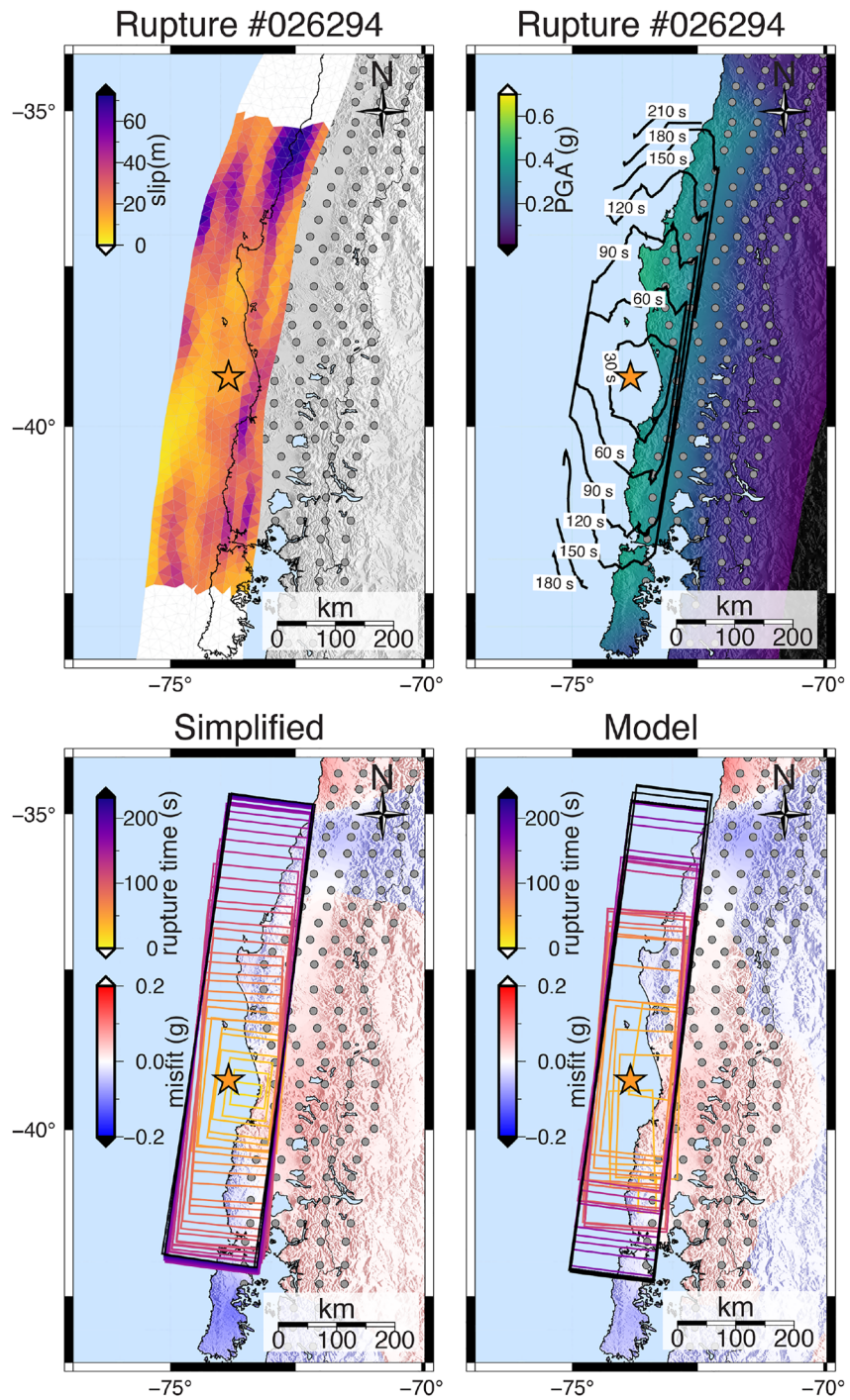
Figure 5. Example rupture scenario, model objective, shake maps and their residuals. A fault rupture is first simplified by the rectangular fault, as represented by Mw, centroid location, and rupture extent. The M-LARGE model aims to match the simplified fault. Shake maps are calculated from the Chilean GMM (Montalva et al., 2017). Residuals are calculated for both the simplified and the model predicted fault. The misfits are calculated by Equation 1. Gray circles mark the location of 525 virtual stations that are used to quantify the prediction performance. Note that some stations are cut-off from the map.

The results of the evaluation at various time intervals are shown in Figure 7. During the initial stage of the rupture (10 s after the origin), when the data do not yet contain any earthquake signals, M-LARGE makes a prediction based solely on the noise, resulting in an inaccurate prediction (Figure 7a). During the growing stage (30 and 60s after origin time), as more stations experience and record deformation from the rupture, M-LARGE corrects
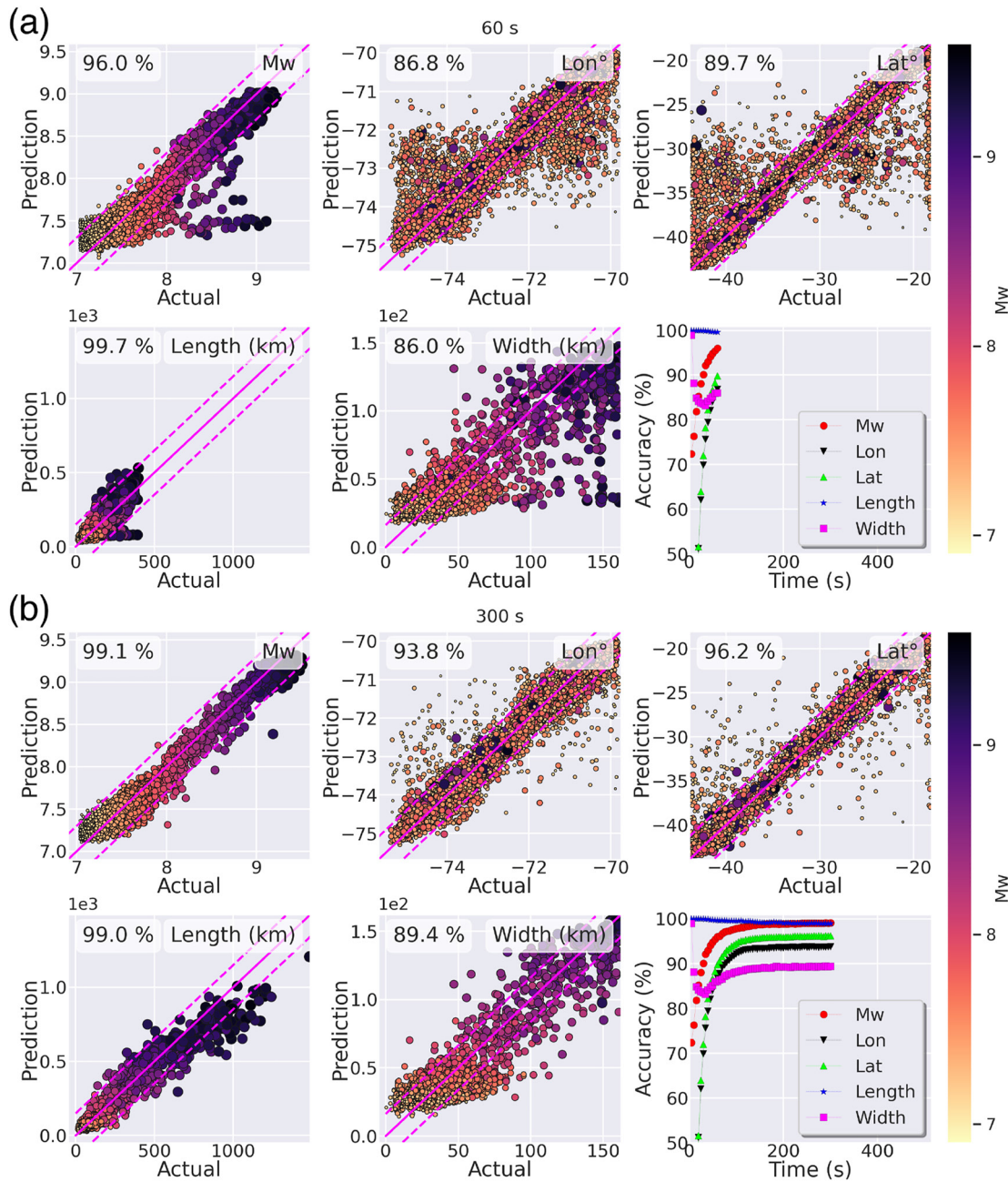
Figure 6. Source parameter predictions on 10,000 unexposed testing data at (a) 60 s and (b) 300 s after the origin. Colored dots show the predicted and true values at their respective times. Magenta lines mark the boundary of accuracy estimation, defined by ±10% of the parameter range (i.e., maximum-minimum value of the labels). The accuracy plot shows the overall parameter performance as a function of time.

the centroid location and expands the fault (Figures 7b and 7c). By 510 s after the origin (the final stage), most stations have already received the rupture signals and the predicted source parameters do not change significantly from 60 s after the origin. These results are consistent with those reported by Lin et al. (2021). Similarly, the performance of the other four Chilean earthquakes are shown in Figures S5–S8 in Supporting Information S1.

Our model successfully predicts the source parameters for all the Chilean earthquakes except for the 2016 Mw7.6 Melinka earthquake, where the centroid is slightly biased. This is not surprising due to the imperfect conditions with large GNSS noise and sparse station coverage, as demonstrated in Figure S3 in Supporting Information S1. This provides us valuable insights into areas where further enhancement is needed, and by understanding the challenges, we are more prepared to address them effectively for future earthquakes.
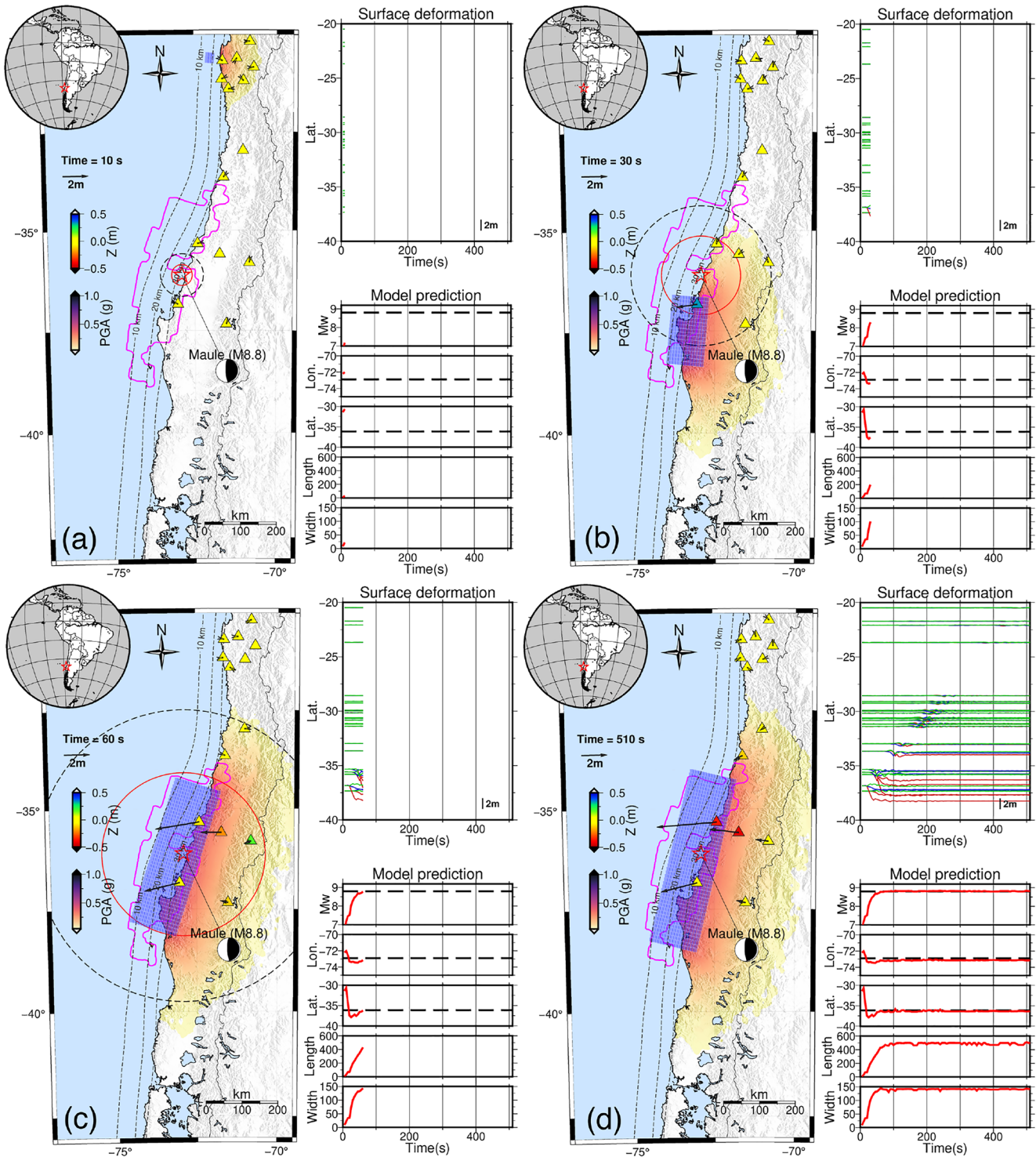
Figure 7. M-LARGE performance on real data: the 2010 Mw8.8 Maule earthquake. Gray triangles mark the Chilean HR-GNSS stations that were not operating or unavailable during the earthquake. Colored triangles show the available stations, color coded by their vertical displacement value. Shading of the map shows the PGA prediction based on the predicted fault (blue rectangle) by the Chilean GMM (Montalva et al., 2017), and the small arrows on the triangles denote coseismic displacement at the time. Magenta line marks the finite fault solution from the U.S. Geological Survey. Black dashed line and red solid lines show the expected P and S arrival, respectively. (a) Initial stage of the rupture (10 s), where none of the stations have yet experienced deformation or shaking. (b)–(c) Growing stage of the rupture (30 and 60 s). (d) Final stage of the rupture (510 s i.e., the maximum time for model testing).
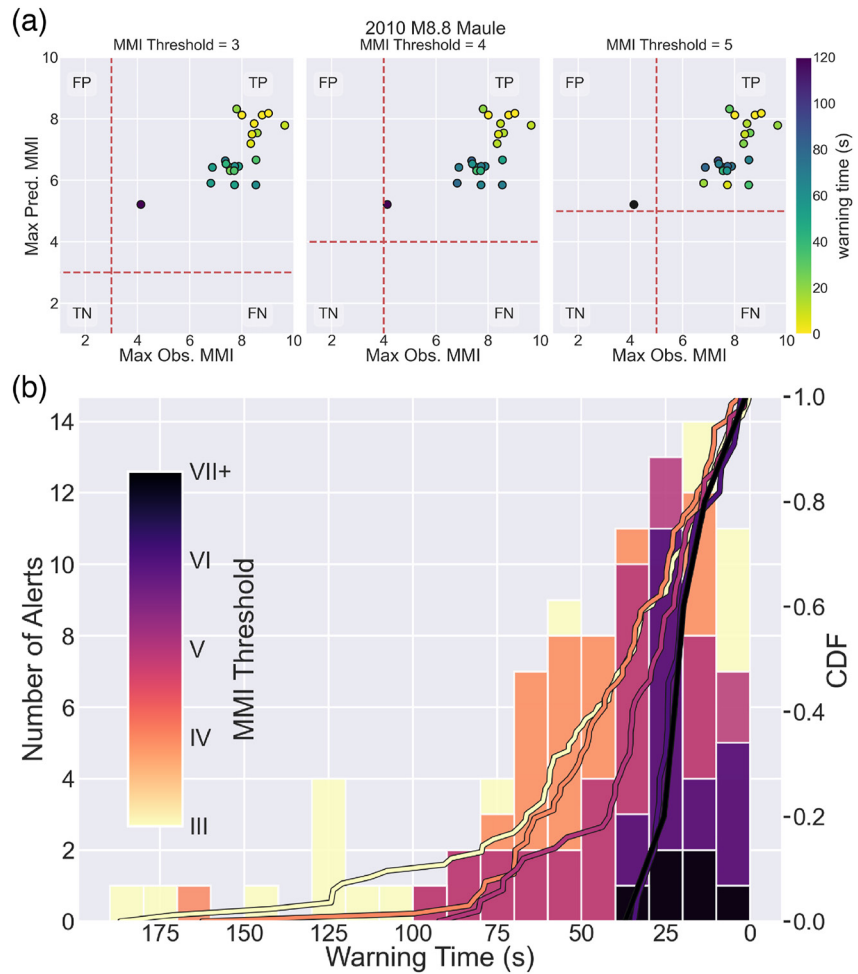
Figure 8. M-LARGE prediction on real data. The five large Chilean earthquakes are shown in Figure 1. (a) Warning time for 2010 M8.8 Maule with MMI level of 3, 4, and 5. (b) Histograms of all the alerts from five large Chilean earthquakes with different MMI levels and their cumulative distribution function (CDF), colored by their MMI.

4.3. Timeliness of Alerts

The ultimate goal of the rapid source prediction is to forecast shaking intensity. To understand the timeliness of warnings, we first compare the M-LARGE predicted GM to the real GM records of the 2010 M8.8 Maule earthquake collected from Ruhl et al. (2019). We calculate the effective warning time, defined as when the prediction is faster than the actual onset at a particular MMI level, to evaluate the performance (Figure 8a). We find that M-LARGE can provide accurate MMI prediction and significant warning time for most of the sites. For MMI = 4 as example, it shows 100% true positive predictions, and a warning time of 30–60 s for most of the MMI < 7 stations (Figure 8a). For MMI ≥ 8, some stations provide less or no warning time because these stations are close to the source (~100 km) and located in the blind zone of the model where only a few GNSS stations were operating during 2010 (Figure 7).

Similarly, we calculate the warning time for all the other Chilean large earthquakes (Figure 1) at various MMI levels (Figure 8b). The warning times for these events are shown in the Figures S9–S12 in Supporting Information S1. The result shows a long median warning time of 36 s for MMI = 4, and 28 s for MMI = 5, which is slightly better than the result of Ruhl et al. (2019) of 34 and 26 s for MMI = 4 and MMI = 5, respectively. One major improvement is that our model does not rely on the seismic triggered parameters (i.e., earthquake magnitude and source location) which may introduce latency and magnitude saturation as observed in purely seismic approaches (Allen & Melgar, 2019; Murray et al., 2018). Also, the ability to track the centroid location instead of the hypocenter makes our model more reliable for large, unilateral ruptures which have been proven challenging
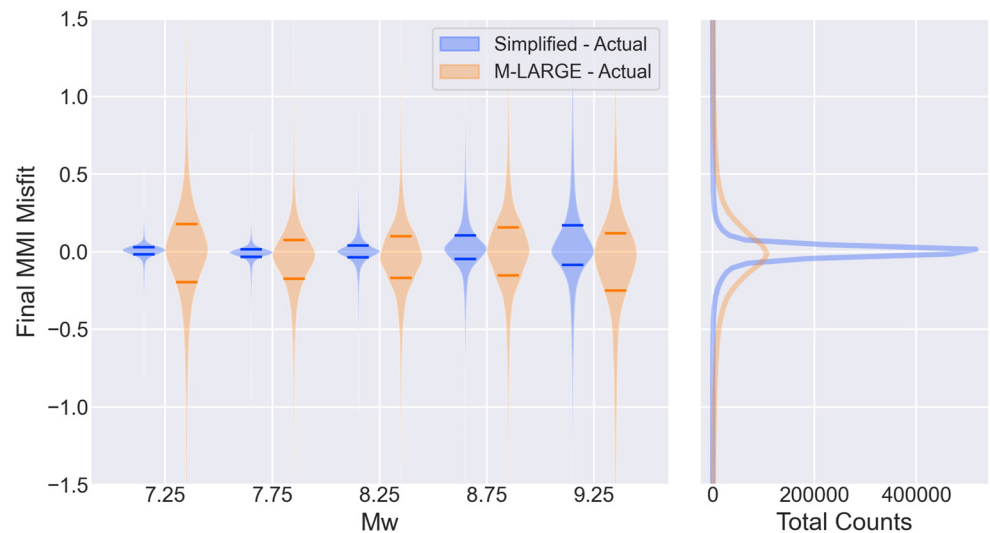
Figure 9. Final MMI misfits at the 525 virtual stations for the simplified and M-LARGE predicted faults in different Mw groups. We take the fault at 510 s as the final fault to generate MMI values. To prevent zero to zero comparison for distant stations, the misfit is only calculated at the stations with the true MMI value ≥3 MMI. The average MMI misfits are -0.002 ± 0.116 and -0.062 ± 0.492, for simplified and M-LARGE predicted, respectively.

(Williamson et al., 2020). Thus, we anticipate that our model can offer a longer and more accurate warning time compared to other similar methods.

5. Discussion

5.1. Error Estimation

The M-LARGE model predicts 5 source parameters as a representation of the actual fault. We discuss whether these parameters are sufficient to accurately reconstruct the finite fault and predict ground motion. To assess the level of misfit introduced by the simplification of the fault geometry, we calculate the differences in shaking intensity in MMI scale between the simplified and actual finite fault (Figure 9) by Equation 1. We compare the misfits at the final time (i.e., 510 s), by which most of the ruptures should be complete. Our result shows an average MMI misfit close to zero and a standard deviation of 0.12 MMI scale. This suggests that the simplified fault plane can be used as the finite fault and the difference in MMI estimates is minimal.

We further evaluate the M-LARGE prediction error by comparing the model predictions with the actual MMI values. Similarly, we calculate the final MMI misfits based on the M-LARGE predicted source parameters and the actual fault (Figure 9). The analysis indicates that M-LARGE provides an accurate final MMI prediction with an average error of -0.06 and a standard deviation of 0.49 on the MMI scale. Considering the existing 0.1 MMI misfit due to the fault simplification error, the overall error is relatively small, suggesting that our M-LARGE model can accurately predict actual GM. The timeliness analysis will further explore this evaluation by comparing the M-LARGE predicted MMI time series with the actual MMI time series from high-frequency synthetic data in the following section (Section 5.2).

5.2. Overall Warning Time Performance

To evaluate the overall warning time performance of our M-LARGE model, we analyze the warning time with the 10,000 earthquakes from the testing data set. The data set comprises a larger range of earthquake magnitudes (Mw7.0–9.5) and events with larger rupture extent (i.e., 1,000+ km) than the real Chilean earthquake data set we have shown in Section 4.3. We compare the M-LARGE predicted ground motion with the synthetic high-frequency broadband data and calculate the effective warning time. Our results show that, with the rapid estimation of earthquake sources, our model yields a median warning time of 34.5 s for all the MMI levels for a distance of 200 km, which increases to 58.4 s for sites with a distance of 300 km (Figure 10). The warning time at
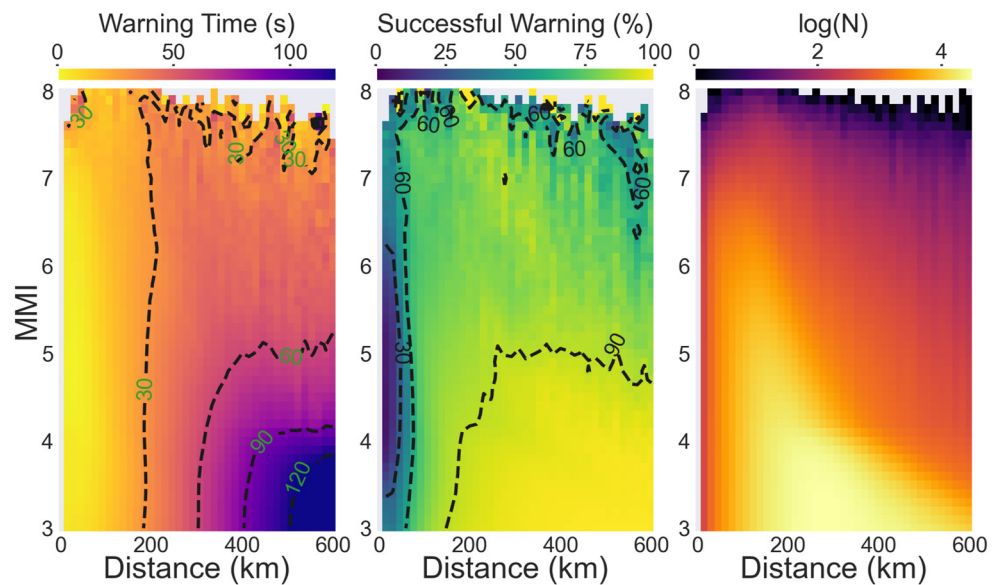
Figure 10. Overall warning time statistic of the M-LARGE model. The analysis is performed on 10,000 simulated earthquakes and synthetic waveforms. Warning time is accessed by the median value of all the effective warnings at a particular distance and MMI level. The total waveform number N is shown in the logarithm scale.

200 km is similar to what was reported by Ruhl et al. (2019), but it is important to note that our model has higher flexibility for those large magnitude events that have previously proven challenging for existing EEW models (e.g., Allen and Melgar (2019)). Additionally, taking into account a blind zone of 100 km due to the subduction zone geometry and the sparse distribution of the GNSS stations (e.g., the case in Figure 7), where only a few stations record at the initial stage, this is a relatively long warning time and can provide meaningful strong motion warning before its onset. For MMI = 4, our model yields a long median warning time of 40.5 s, which decreases to 25.8 s for MMI = 5, similar to the performance of the real data test.

Finally, we analyze the warning time statistic by calculating the successful warning rate:

$$\text{Successful Warning}(\%) = \frac{N_{\text{eff}}}{N_{\text{eff}} + N_{\text{late}}} \times 100\% \tag{2}$$

where N_{eff} and N_{late} represent the number of effective warnings and the number of late warnings, respectively. The result shows a high successful warning rate for most of the sites, suggesting that our model can provide long and accurate GM forecasting.

5.3. Limitations and Future Improvements

We show that the HR-GNSS data quality and extent of station coverage have a significant impact on the accuracy of the model. Specifically, we observe large misfits in source prediction in areas with poor station coverage, such as the peripheries of the subduction zone (e.g., 2016 Mw7.6 Melinka earthquake as shown in Figure S8 in Supporting Information S1). To improve the performance in these regions, we propose two potential strategies: increasing the number of HR-GNSS stations or incorporating seismic data into the model. Seismic data can provide accurate arrival time as an important constraint to the source location. Although this information can differ from the centroid location, it is typically comparable for smaller magnitude events. Our result on the warning time also highlights the importance of adding observations closer to the trench. For example, in the 2010 Mw8.8 Maule earthquake, there were no rupture signals that arrived within the first 15 s of the data. This could be significantly improved with the recent endeavor of seafloor geodesy or nontraditional data (e.g., Lindsey et al., 2017; Allen & Melgar, 2019). Lastly, our model has demonstrated the ability to learn earthquake scaling from synthetic data, and that this knowledge can be applied to unseen real data. This suggests that our understanding of earthquake rupture is, to first order, consistent with reality. Because the model relies fully on synthetic data, any future advancements in earthquake source theory or velocity structure will help us to improve the model performance by incorporating

more realistic simulations. Recently, for example, Fadugba et al. (2023) showed that simulations with real 3D subduction zone structure provide far better results when simulating HR-GNSS waveforms than the simplified 1D structure assumption. This points toward an obvious direction for further improving our model performance. Our findings emphasize the need to consider data quality, station distribution, observation location, and realistic assumptions in simulating earthquakes for accurate and rapid EEW performance.

6. Conclusion

In this paper, we propose a modified M-LARGE model (Lin et al., 2021) that predicts finite fault parameters for large earthquakes from surface displacement patterns from HR-GNSS data. We test the new model with synthetic and real data in the past 13 years in the Chilean Subduction Zone and show that it successfully predicts magnitude with a high accuracy of 99% and an average of 95% for other source parameters. These predictions can be used to further forecast strong ground motion. Our synthetic earthquakes test suggests that a long median warning time of 34.5 s can be made at the sites with hypocentral distance of 200 km, and this increases to 58.4 s for distance 300 km. Additionally, both the synthetic data and real Chilean earthquake data test provide a longer warning time of 36~40.5 s at sites with MMI = 4, longer than the existing G-larmS algorithm of 34 s. Most importantly, the prediction does not rely on seismic methods which will potentially introduce latency and saturated information from the seismic approaches. We conclude that the M-LARGE model can be utilized to generate timely forecasts of ground motion, and it can be employed alongside with other methods to augment the overall effectiveness of EEW systems.

Data Availability Statement

The rupture simulations and waveforms are obtained from Zenodo: https://zenodo.org/record/5015610#. ZHaAMOzMInc (Lin et al., 2020). Details about data and Fakequake source code can be found in Melgar et al. (2016) and Lin et al. (2021). Codes of M-LARGE can be found at https://zenodo.org/record/4527253#. ZHaA6ezMInc (Lin, 2021).

References

Abercrombie, R. E. (1995). Earthquake source scaling relationships from− 1 to 5 ML using seismograms recorded at 2.5-km depth. *Journal of Geophysical Research*, *100*(B12), 24015–24036. https://doi.org/10.1029/95jb02397

Aki, K. (1967). Scaling law of seismic spectrum. *Journal of Geophysical Research*, *72*(4), 1217–1231. https://doi.org/10.1029/jz072i004p01217

Allen, R. M. (2007). The ElarmS earthquake early warning methodology and application across California. In P. Gasparini, G. Manfredi, & J. Zschau (Eds.), *Earthquake early warning systems*. Springer. https://doi.org/10.1007/978-3-540-72241-0_3

Allen, R. M., & Kanamori, H. (2003). The potential for earthquake early warning in southern California. *Applied Physics Letters*, *293*(9). https://www.science.org

Allen, R. M., & Melgar, D. (2019). Earthquake early warning: Advances, scientific challenges, and societal needs. *Annual Review of Earth and Planetary Sciences*, *47*(1), 361–388. https://doi.org/10.1146/annurev-earth-053018-060457

Allen, T. I., & Wald, D. J. (2009). On the use of high-resolution topographic data as a proxy for seismic site conditions (VS 30). *Bulletin of the Seismological Society of America*, *99*(2A), 935–943. https://doi.org/10.1785/0120080255

Baez, J. C., Leyton, F., Troncoso, C., del Campo, F., Bevis, M., Vigny, C., et al. (2018). The Chilean GNSS network: Current status and progress toward early warning applications. *Seismological Research Letters*, *89*(4), 1546–1554. https://doi.org/10.1785/0220180011

Blaser, L., Krüger, F., Ohrnberger, M., & Scherbaum, F. (2010). Scaling relations of earthquake source parameter estimates with special focus on subduction environment. *Bulletin of the Seismological Society of America*, *100*(6), 2914–2926. https://doi.org/10.1785/0120100111

Bock, Y., & Melgar, D. (2016). Physical applications of GPS geodesy: A review. *Reports on Progress in Physics*, *79*(10), 106801. https://doi.org/10.1088/0034-4885/79/10/106801

Boore, D. M., & Bommer, J. J. (2005). Processing of strong-motion accelerograms: Needs, options and consequences. *Soil Dynamics and Earthquake Engineering*, *25*(2), 93–115. https://doi.org/10.1016/j.soildyn.2004.10.007

Böse, M., Heaton, T. H., & Hauksson, E. (2012). Real-time finite fault rupture detector (FinDer) for large earthquakes. *Geophysical Journal International*, *191*(2), 803–812. https://doi.org/10.1111/j.1365-246x.2012.05657.x

Böse, M., Ionescu, C., & Wenzel, F. (2007). Earthquake early warning for Bucharest, Romania: Novel and revised scaling relations. *Geophysical Research Letters*, *34*(7), L07302. https://doi.org/10.1029/2007gl029396

Böse, M., Smith, D. E., Felizardo, C., Meier, M. A., Heaton, T. H., & Clinton, J. F. (2018). FinDer v. 2: Improved real-time ground-motion predictions for M2–M9 with seismic finite-source characterization. *Geophysical Journal International*, *212*(1), 725–742. https://doi.org/10.1093/gji/ggx430

Chung, A. I., Meier, M. A., Andrews, J., Böse, M., Crowell, B. W., McGuire, J. J., & Smith, D. E. (2020). ShakeAlert earthquake early warning system performance during the 2019 Ridgecrest earthquake sequence. *Bulletin of the Seismological Society of America*, *110*(4), 1904–1923. https://doi.org/10.1785/0120200032

Cochran, E. S., Bunn, J., Minson, S. E., Baltay, A. S., Kilb, D. L., Kodera, Y., & Hoshiba, M. (2019). Event detection performance of the PLUM earthquake early warning algorithm in southern California. *Bulletin of the Seismological Society of America*, *109*(4), 1524–1541. https://doi.org/10.1785/0120180326

Crowell, B. W., Melgar, D., Bock, Y., Haase, J. S., & Geng, J. (2013). Earthquake magnitude scaling using seismogeodetic data. *Geophysical Research Letters*, *40*(23), 6089–6094. https://doi.org/10.1002/2013gl058391

Crowell, B. W., Schmidt, D. A., Bodin, P., Vidale, J. E., Gomberg, J., Renate Hartog, J., et al. (2016). Demonstration of the Cascadia G-FAST geodetic earthquake early warning system for the Nisqually, Washington, earthquake. *Seismological Research Letters*, *87*(4), 930–943. https://doi.org/10.1785/0220150255

Ekström, G., Nettles, M., & Dziewoński, A. M. (2012). The global CMT project 2004–2010: Centroid-moment tensors for 13,017 earthquakes. *Physics of the Earth and Planetary Interiors*, *200*, 1–9. https://doi.org/10.1016/j.pepi.2012.04.002

Espinosa-Aranda, J. M., Cuellar, A., Garcia, A., Ibarrola, G., Islas, R., Maldonado, S., & Rodriguez, F. H. (2009). Evolution of the Mexican seismic alert system (SASMEX). *Seismological Research Letters*, *80*(5), 694–706. https://doi.org/10.1785/gssrl.80.5.694

Espinosa Aranda, J. M., Jimenez, A., Ibarrola, G., Alcantar, F., Aguilar, A., Inostroza, M., & Maldonado, S. (1995). Mexico City seismic alert system. *Seismological Research Letters*, *66*(6), 42–53. https://doi.org/10.1785/gssrl.66.6.42

Fadugba, O. I., Sahakian, V., Melgar, D., Rodgers, A., & Shimony, R. (2023). The impact of the three-dimensional structure of a subduction zone on time-dependent crustal deformation measured by HR-GNSS. *EarthArxiv*. https://doi.org/10.31223/X5PD5N

Given, D. D., Cochran, E. S., Heaton, T., Hauksson, E., Allen, R., Hellweg, P., et al. (2014). *Technical implementation plan for the ShakeAlert production system: An earthquake early warning system for the west coast of the United States* (p. 25). US Department of the Interior, US Geological Survey.

Goldberg, D. E., & Melgar, D. (2020). Generation and validation of broadband synthetic P waves in semistochastic models of large earthquakes. *Bulletin of the Seismological Society of America*, *110*(4), 1982–1995. https://doi.org/10.1785/0120200049

Grapenthin, R., Johanson, I. A., & Allen, R. M. (2014). Operational real-time GPS-enhanced earthquake early warning. *Journal of Geophysical Research: Solid Earth*, *119*(10), 7944–7965. https://doi.org/10.1002/2014jb011400

Graves, R., & Pitarka, A. (2015). Refinements to the Graves and Pitarka (2010) broadband ground-motion simulation method. *Seismological Research Letters*, *86*(1), 75–80. https://doi.org/10.1785/0220140101

Graves, R. W., & Pitarka, A. (2010). Broadband ground-motion simulation using a hybrid approach. *Bulletin of the Seismological Society of America*, *100*(5A), 2095–2123. https://doi.org/10.1785/0120100057

Hayes, G. P. (2017). The finite, kinematic rupture properties of great-sized earthquakes since 1990. *Earth and Planetary Science Letters*, *468*, 94–100. https://doi.org/10.1016/j.epsl.2017.04.003

Hoshiba, M., Iwakiri, K., Hayashimoto, N., Shimoyama, T., Hirano, K., Yamada, Y., et al. (2011). Outline of the 2011 off the Pacific coast of tohoku earthquake (Mw 9.0)—Earthquake early warning and observed seismic intensity. *Earth Planets and Space*, *63*(7), 547–551. https://doi.org/10.5047/eps.2011.05.031

Hoshiba, M., & Ozaki, T. (2014). Earthquake early warning and tsunami warning of the Japan MeteorologicalAgency, and their performance in the 2011 off the Pacific coast of Tohoku earthquake (M9.0). In F. Wenzel & J. Zschau (Eds.), *EarlyWarning for geological disasters* (pp. 1–28). Springer-Verlag.

Hsiao, N. C., Wu, Y. M., Shin, T. C., Zhao, L., & Teng, T. L. (2009). Development of earthquake early warning system in Taiwan. *Geophysical Research Letters*, *36*(5), L00B02. https://doi.org/10.1029/2008gl036596

Hutchison, A. A., Böse, M., & Manighetti, I. (2020). Improving early estimates of large earthquake's final fault lengths and magnitudes leveraging source fault structural maturity information. *Geophysical Research Letters*, *47*(14), e2020GL087539. https://doi.org/10.1029/2020gl087539

Jozinović, D., Lomax, A., Štajduhar, I., & Michelini, A. (2020). Rapid prediction of earthquake ground shaking intensity using raw waveform data and a convolutional neural network. *Geophysical Journal International*, *222*(2), 1379–1389. https://doi.org/10.1093/gji/ggaa233

Kamigaichi, O., Saito, M., Doi, K., Matsumori, T., Tsukada, S. Y., Takeda, K., et al. (2009). Earthquake early warning in Japan: Warning the general public and future prospects. *Seismological Research Letters*, *80*(5), 717–726. https://doi.org/10.1785/gssrl.80.5.717

Kodera, Y., Yamada, Y., Hirano, K., Tamaribuchi, K., Adachi, S., Hayashimoto, N., et al. (2018). The propagation of local undamped motion (PLUM) method: A simple and robust seismic wavefield estimation approach for earthquake early WarningThe propagation of local undamped motion (PLUM) method. *Bulletin of the Seismological Society of America*, *108*(2), 983–1003. https://doi.org/10.1785/0120170085

Kuang, W., Yuan, C., & Zhang, J. (2021). Real-time determination of earthquake focal mechanism via deep learning. *Nature Communications*, *12*(1), 1432. https://doi.org/10.1038/s41467-021-21670-x

Larson, K. M. (2009). GPS seismology. *Journal of Geodesy*, *83*(3–4), 227–233. https://doi.org/10.1007/s00190-008-0233-x

Lin, J. T. (2021). jiunting/MLARGE: First release of MLARGE (Version v1.0.0) [Software]. Zenodo. https://doi.org/10.5281/zenodo.4527253

Lin, J. T., Melgar, D., Thomas, A., & Searcy, J. (2020). Chilean subduction zone rupture scenarios and waveform data [Dataset]. Zenodo. https://doi.org/10.5281/zenodo.5015610

Lin, J. T., Melgar, D., Thomas, A. M., & Searcy, J. (2021). Early warning for great earthquakes from characterization of crustal deformation patterns with deep learning. *Journal of Geophysical Research: Solid Earth*, *126*(10), e2021JB022703. https://doi.org/10.1029/2021jb022703

Lindsey, N. J., Martin, E. R., Dreger, D. S., Freifeld, B., Cole, S., James, S. R., et al. (2017). Fiber-optic network observations of earthquake wavefields. *Geophysical Research Letters*, *44*(23), 11–792. https://doi.org/10.1002/2017gl075722

Lomax, A., Michelini, A., & Jozinović, D. (2019). An investigation of rapid earthquake characterization using single-station waveforms and a convolutional neural network. *Seismological Research Letters*, *90*(2A), 517–529. https://doi.org/10.1785/0220180311

Meier, M. A. (2017). How "good" are real-time ground motion predictions from earthquake early warning systems? *Journal of Geophysical Research: Solid Earth*, *122*(7), 5561–5577. https://doi.org/10.1002/2017jb014025

Melgar, D., Crowell, B. W., Melbourne, T. I., Szeliga, W., Santillan, M., & Scrivner, C. (2020). Noise characteristics of operational real-time high-ate GNSS positions in a large aperture network. *Journal of Geophysical Research: Solid Earth*, *125*(7), e2019JB019197. https://doi.org/10.1029/2019jb019197

Melgar, D., LeVeque, R. J., Dreger, D. S., & Allen, R. M. (2016). Kinematic rupture scenarios and synthetic displacement data: An example application to the Cascadia subduction zone. *Journal of Geophysical Research: Solid Earth*, *121*(9), 6658–6674. https://doi.org/10.1002/2016jb013314

Minson, S. E., Baltay, A. S., Cochran, E. S., Hanks, T. C., Page, M. T., McBride, S. K., et al. (2019). The limits of earthquake early warning accuracy and best alerting strategy. *Scientific Reports*, *9*(1), 2478. https://doi.org/10.1038/s41598-019-39384-y

Minson, S. E., Murray, J. R., Langbein, J. O., & Gomberg, J. S. (2014). Real-time inversions for finite fault slip models and rupture geometry based on high-rate GPS data. *Journal of Geophysical Research: Solid Earth*, *119*(4), 3201–3231. https://doi.org/10.1002/2013jb010622

Montalva, G. A., Bastías, N., & Rodriguez-Marek, A. (2017). Ground-motion prediction equation for the Chilean subduction zone. *Bulletin of the Seismological Society of America*, *107*(2), 901–911. https://doi.org/10.1785/0120160221

Mousavi, S. M., & Beroza, G. C. (2020). A machine-learning approach for earthquake magnitude estimation. *Geophysical Research Letters*, *47*(1), e2019GL085976. https://doi.org/10.1029/2019gl085976